



The Synthesis and Characterization of Hard-Soft $\text{Mn}_{52}\text{Al}_{45.7}\text{C}_{2.3}\text{-}\alpha\text{-Fe}$ Nanocomposite Magnets

S. N. Attyabi¹ · S. M. A. Radmanesh¹ · S. A. Seyyed Ebrahimi¹ · H. Dehghan¹

Received: 6 July 2021 / Accepted: 24 January 2022 / Published online: 21 February 2022
© The Author(s), under exclusive licence to Springer Science+Business Media, LLC, part of Springer Nature 2022

Abstract

We report on the magnetic exchange coupling behavior in hard-soft $\text{Mn}_{52}\text{Al}_{45.7}\text{C}_{2.3}\text{-}\alpha\text{-Fe}$ nanocomposite magnets synthesized by high-energy ball milling at room temperature followed by post-annealing treatment at temperatures 300 to 600 °C. The analysis of hysteresis loops showed effective exchange coupling $\text{Mn}_{52}\text{Al}_{45.7}\text{C}_{2.3}\text{-}\alpha\text{-Fe}$ nanocomposite particles with smooth demagnetizing curves when annealed at 400 °C. But higher annealing temperatures pose kink in the hysteresis loop highlighting a weak exchange coupling with more magnetostatic interaction between hard and soft components. This trend was confirmed by the results on $(\text{BH})_{\text{max}}$, which had the highest value for nanocomposite particles annealed at 400 °C. More detailed information on magnetic exchange coupling in nanocomposite particles was obtained by derivative magnetic curves and Henkel plots. Hard-soft $\text{Mn}_{52}\text{Al}_{45.7}\text{C}_{2.3}\text{-}\alpha\text{-Fe}$ magnets showed the sharpest high-field maximum in derivative magnetic curves when annealed at 400 °C as a signature of effective exchange coupling between $\text{Mn}_{52}\text{Al}_{45.7}\text{C}_{2.3}$ and $\alpha\text{-Fe}$ grains. In addition, Henkel plots display the dominance of positive peak for nanocomposite particles annealed at 300 and 400 °C, indicative of magnetic exchange-coupling. But the negative-peak dominated curves of those annealed at higher temperatures as well as single-phase $\text{Mn}_{52}\text{Al}_{45.7}\text{C}_{2.3}$ imply a significant magnetostatic interaction in the components owing to non-magnetic phases formed at elevated temperatures. Also, quantitative information obtained from recoil curve measurements assigned a higher degree of exchange coupling to nanocomposite magnets when annealed at 400 °C.

Keywords Permanent magnets · Magnetic exchange coupling · $(\text{BH})_{\text{max}}$ · High energy ball milling · Magnetostatic interaction · Magnetization reversal behavior

1 Introduction

The development and integration of high-performance permanent magnets are now well established in the research about high functional materials for desirable application like renewable power generation, eco-technologies and so on [1–3]. It is noteworthy that technological application extensively benefits from rare-earth-doped permanent magnets due to the better app response compared with rare-earth-free counterparts [4, 5]. However, issues such as material supply and price among others might inhibit the functionality of rare-earth permanent magnets in green technologies. Hence, permanent magnets with minimum amounts of rare-earth elements seem to be of high interest in new applications [2,

5–7]. Mn-Al alloy as a rare-earth-free permanent magnet has been studied profoundly for the potentially important advantages in required applications [8–10]. According to the phase diagram of Mn-Al, ferromagnetic $\tau\text{-Mn-Al}$ possesses peculiar high uniaxial magnetocrystalline anisotropy. That is because Mn tends for antiferromagnetic contribution in the tetragonal lattice. It has been realized that a delicate adjustment of Mn interatomic distances through Al can render ferromagnetic configuration in $\tau\text{-Mn-Al}$ phase [11, 12]. Many studies on Mn-Al alloys reveal different magnetic properties in terms of H_c and M_s . The highest H_c has been found for ultra-thin films of $t \approx 11$ nm. Also, M_s varies dramatically between 15 and 120 emu g^{-1} . As found experimentally, the ferromagnetic τ phase is thermodynamically metastable that forms through the annealing of nonmagnetic $\varepsilon\text{-Mn-Al}$ phase [3, 12, 13]. Phase transformation embodies too many defects in the lattice structure. The milling process of Mn-Al makes defects in the structure as well. It is worth mentioning that the produced lattice defects favor anti-ferromagnetic

✉ S. A. Seyyed Ebrahimi
saseyyed@ut.ac.ir

¹ Advanced Magnetic Materials Research Center, College of Engineering, University of Tehran, Tehran, Iran

coupling of Mn atoms. This trend escalates with additional amounts of Mn in an optimized Mn–Al alloy [14–17]. As a serious minus, the squareness of hysteresis loop M_r/M_s is low that brings on $(BH)_{\max}$ far below the ideal value of a perfect permanent magnet candidate. Other types of defects such as anti-phases and twins are believed to account for lower energy products in Mn–Al compared to the theoretical value [14–18]. Since it is of prime importance to boost the performance of permanent magnets, lots of efforts have been made in this way to fulfill it. Recently, the field of nanocomposite magnets as integrated systems with complementary components has become very promising in this regard. Particularly, exchange-spring magnets to provide the superior $(BH)_{\max}$ with coherent rotation under reversal field through exploiting the high magnetization of soft phase and high anisotropy of hard phase have been the subject of numerous research works [16, 17, 19–25]. Inter-phase coupling strength in hybrid magnets is measured by the switching field of soft and hard components. The reasons behind low performance of $Mn_{52}Al_{45.7}C_{2.3}$ have been investigated recently using recoil curves to understand $Mn_{52}Al_{45.7}C_{2.3}$ microstructure. The reported work imputes low $(BH)_{\max}$ to the grains of τ phase with a large distribution of K and suggests Mn–Mn antiferromagnetic interaction needs to be minimized for the sake of less anisotropy distribution and reduced intergranular exchange [26]. However, the occurrence of exchange spring behavior in $Mn_{52}Al_{45.7}C_{2.3}$ - α -Fe hybrid nanoparticles has not been investigated so far.

In this article, we study the magnetization reversal of hard-soft $Mn_{52}Al_{45.7}C_{2.3}$ - α -Fe nanocomposites with quite different manifestations of exchange spring behavior to non-exchange spring behavior. Annealing temperature has been varied to investigate these behaviors in nanocomposite particles. Here, using the exchange spring mechanism, we in fact accomplished enhancing the energy product of hybrid nanoparticles compared to $Mn_{52}Al_{45.7}C_{2.3}$. Also, we have used Henkel plots to deeply understand the magnetic exchange coupling in $Mn_{52}Al_{45.7}C_{2.3}$ - α -Fe nanocomposite magnets. These techniques provide indispensable quantitative information on the dominant interaction in our systems. We need to point out that in this work, the switching field distributions in both non-exchange and exchange spring cases have been investigated.

2 Experimental

Mn–Al alloys with nominal composition ($Mn_{52}Al_{45.7}C_{2.3}$) were prepared by a vacuum induction melting procedure. Re-melting process under controlled Ar atmosphere was carried out two times to ensure the homogeneity of the casted alloys as well as to adjust the composition of the obtained parent alloy. It should be noted that a titanium getter system

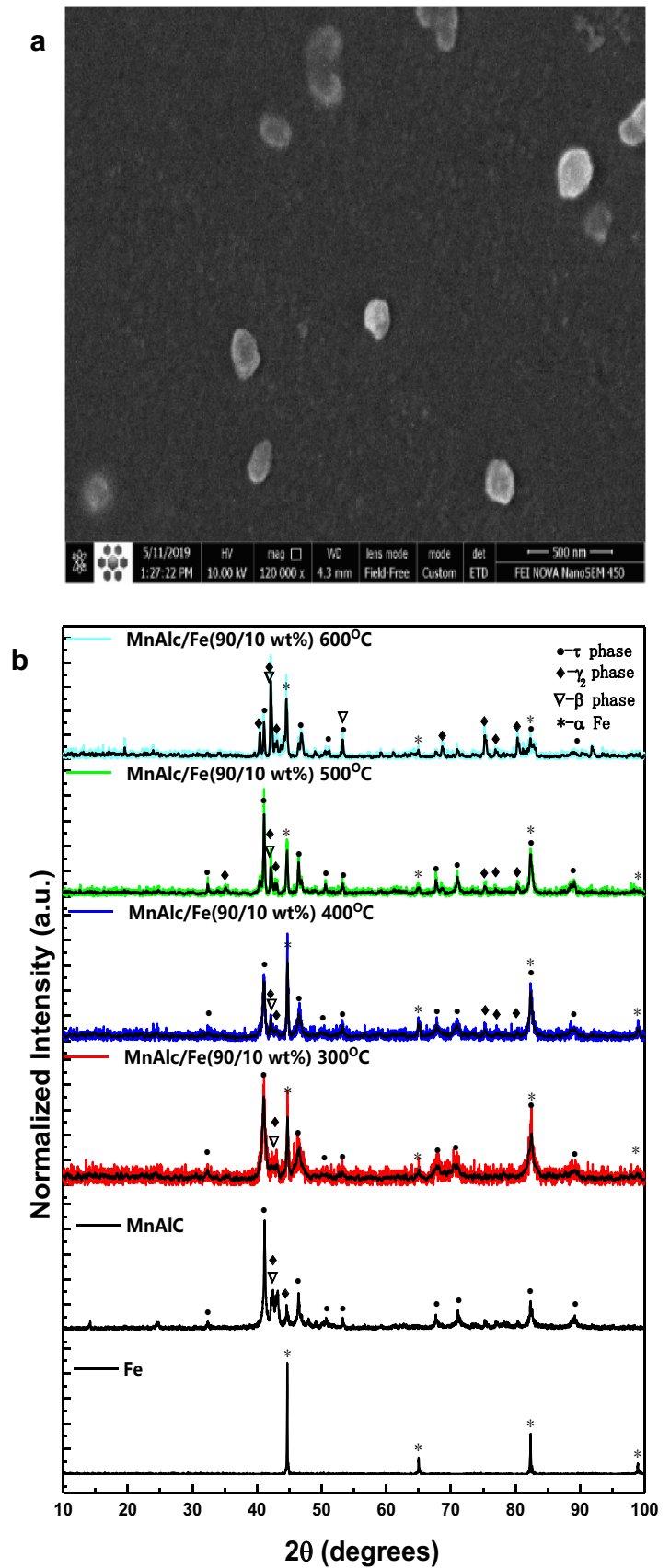
was used to purify the chamber from residual oxygen. The actual composition of casted alloys was tested by inductivity coupled plasma-optical emission spectroscopy (ICP-OES, 730-ES, Varian, USA), and carbon content was measured using LECO CS-244 carbon determinator (ASTM E1019). The final ingots then were crushed and milled for 5 h using high-energy planetary milling. The resulted $Mn_{52}Al_{45.7}C_{2.3}$ powder with a mean particle size of 100 nm was obtained at the end of the process. Mn–Al–C powders were then mixed with 10 Wt% α -Fe powder. The mixture was mechanically milled in cyclohexane medium for 1 h to reach a homogeneous composite powder. Then, it was put into a tungsten carbide die with a 5-mm diameter and pressed under a uniaxial constant pressure of 5.1 GPa. Afterward, the obtained bulk samples were annealed in a vacuum tube furnace at temperatures of 300, 400, 500, and 600 °C for 30 min to optimize the magnetic properties. That was to investigate the role of the heat treatment period on magnetic properties of nanostructured bulk magnets. It is noteworthy that the α -Fe powder of nano-size (35–45 nm) has been used in the experiments. The microstructure of the alloys was determined by x-ray diffractometer Rigaku Ultima IV with Cu- K_{α} lamp. Metallographic studies were conducted by optical microscope OLYMPUS PMG3 and scanning electron microscope TESCAN SEM. The magnetization reversal behavior of the alloys was investigated by a vibrating sample magnetometer, MagKavCo.

3 Results and Discussion

Figure 1a shows FESEM images of $Mn_{52}Al_{45.7}C_{2.3}$ samples mechanically ball milled for 5 h. The morphology of $Mn_{52}Al_{45.7}C_{2.3}$ particles was also studied that reveals the particles are spherical or elliptic. In addition, the average particle size of 100 nm was determined using ImageJ technique.

In Fig. 1b, XRD patterns of initial specimens of $Mn_{52}Al_{45.7}C_{2.3}$ and Fe nanopowders have been illustrated. It should be noted that XRD patterns of $Mn_{52}Al_{45.7}C_{2.3}$ -10% Fe nanocomposites are attributed to the samples that had undergone high-energy ball milling for 1 h which were then pressed and sintered at 300 to 600 °C. It can be verified that the diffracted peaks of sintered samples at 300 and 400 °C are consistent with τ and α -Fe phases. When the temperature rises to 400 °C, the strain in samples diminishes that leads to a higher atomic order in the structure. On the other hand, at higher temperatures, τ phase decomposes to β and γ_2 . As seen from XRD patterns, the corresponding peaks of τ phase in the nanocomposite sample sintered at 300 and 400 °C are wider than those of mechanically milled nanopowder. Based upon Rietveld analysis [24], extra milling of the composite sample inhibits the contribution of the grain size in

Fig. 1 **a** SEM image of $\text{Mn}_{52}\text{Al}_{45.7}\text{C}_{2.3}$ hard phase and **b** XRD patterns of α -Fe, $\text{Mn}_{52}\text{Al}_{45.7}\text{C}_{2.3}$ and $\text{Mn}_{52}\text{Al}_{45.7}\text{C}_{2.3}$ - α -Fe nanocomposite magnets annealed at 300–600 °C



peak broadening at 300 and 400°. While sintering releases strains trapped in the lattice, the characteristic peak narrows at temperatures higher than 400 °C which is a signature of larger grain size.

The variation of c/a ratio in nanocomposite samples may be ascribed to the enhanced structural order and change in the composition of $\text{Mn}_{52}\text{Al}_{45.7}\text{C}_{2.3}$ τ phase displayed in Fig. 2a. Additionally, at temperatures up to 400 °C, trapped strains in the lattice are released that give rise to volume reduction, while at higher temperatures, this situation gives rise to volume increase due to higher atomic mobility (see Table 1) [27].

The relative long-range order parameter for τ and α -Fe phases, S , was calculated from the comparison of the relative

peak intensity for superlattice ($h+k+l=\text{odd}$) and base structure ($h+k+l=\text{even}$) as follows [27]:

$$S = \sqrt{\frac{\left(\frac{I_s}{I_f}\right)_{dis}}{\left(\frac{I_s}{I_f}\right)_{ord}}} \quad (1)$$

In which $\left(\frac{I_s}{I_f}\right)_{dis}$ and $\left(\frac{I_s}{I_f}\right)_{ord}$ are related to the reflectance intensity ratio for superlattice and base structure in disordered and ordered states, respectively. It is worth mentioning that superlattice (100) and base (101) have been selected in defining S . For accuracy in calculating the S parameter, base peak (101) has been used as base peak (200)

Fig. 2 **a** The tetragonality of c/a ratio and volume of the lattice vs annealing temperature. **b** The ordering parameter, S , and packing factor as a function of the annealing temperature

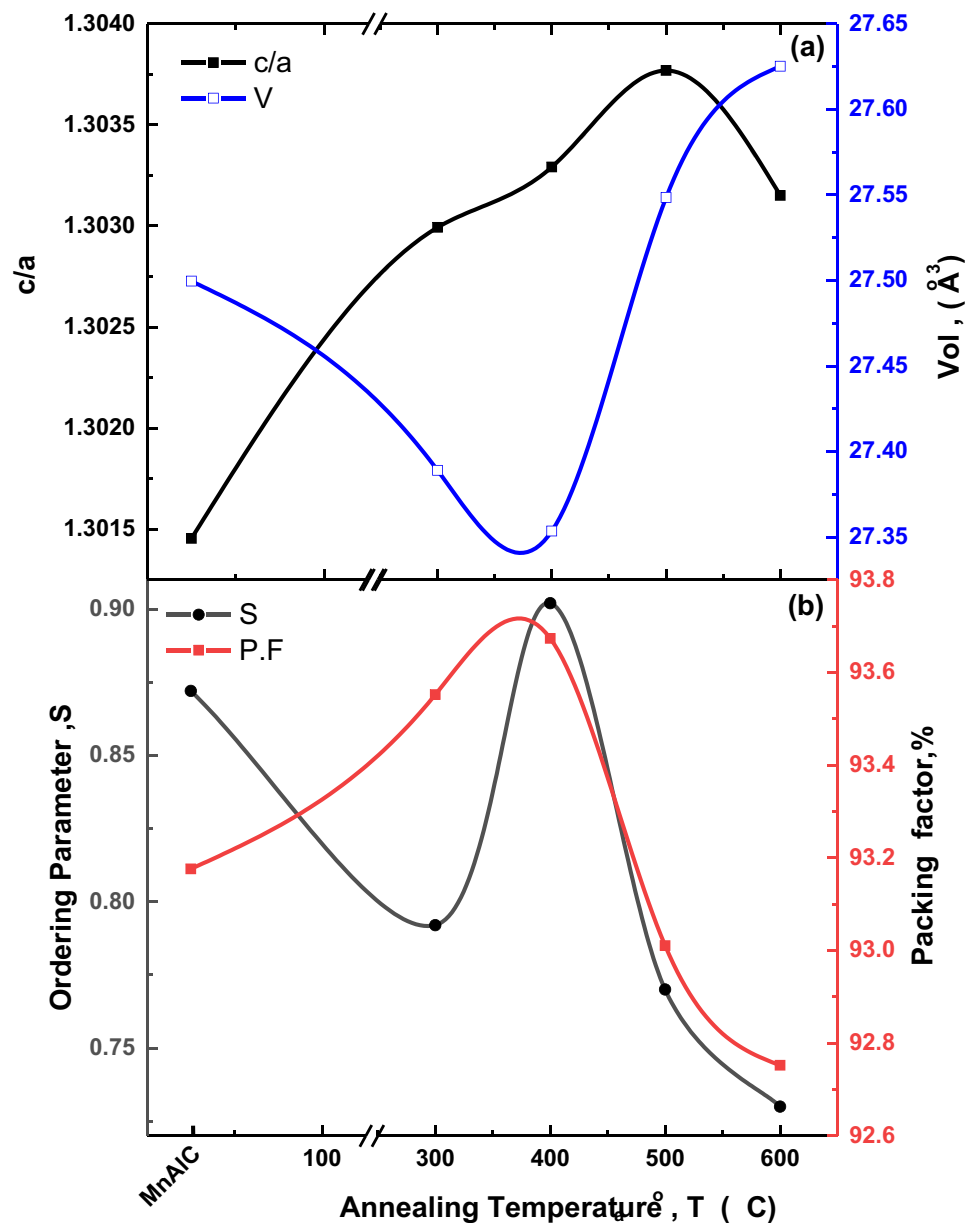


Table 1 Dependence of lattice parameters, crystallite size, and strain on the annealing temperature for Mn–Al–C– α -Fe nanocomposites

Sample	Phase	Lattice parameter [Å] \pm 0.001	V [Å ³]	C/a	P.F [%]	s	Crystallite size [nm]	Strain
MnAlC	τ	$a=2.764$ $c=3.598$	27.487	1.301	93.17	0.872	57.92	0.301
Fe	α -Fe	$a=2.866$	–	–	–	–	24.64	–
MnAlC/Fe (90/10 wt%) 300 °C	τ	$a=2.759$ $c=3.596$	27.373	1.3033	93.55	0.783	32.2	0.059
MnAlC/Fe (90/10 wt%) 400 °C	α -Fe	$a=2.865$	–	–	–	–	23.59	0.081
	τ	$a=2.758$ $c=3.595$	27.345	1.3034	93.67	0.902	42.26	0.042
MnAlC/Fe (90/10 wt%) 500 °C	α -Fe	$a=2.867$	–	–	–	–	31.28	0.056
	τ	$a=2.764$ $c=3.604$	27.533	1.3039	93.01	0.770	176.5	0.003
MnAlC/Fe (90/10 wt%) 600 °C	α -Fe	$a=2.868$	–	–	–	–	46.40	0
	τ	$a=2.767$ $c=3.606$	27.608	1.3032	92.75	0.730	240	0
	α -Fe	$a=2.867$	–	–	–	–	52.34	0

intensity is too weak (see Fig. 2b). S increases with temperature up to 400 °C and then decreases (Fig. 2b). In addition, the crystal structure of τ -phase, cell volume, the axial c/a , and order parameter S as functions of the annealing temperature have been presented (see Table 1; Fig. 2). For Mn–Al–C sample in pre-annealed condition, the values of a^2c and c/a are 27.499 Å and 1.301 Å, respectively, substantially larger than the corresponding values of 27.39 Å and 1.288 Å for the conventional τ -phase [28]. This is due to higher amount of carbon. Temperatures higher than 400 °C alter the tetragonality ratio c/a , leading to lower packing factor in the crystal. That likely escalates the atomic diffusion and subsequently modulates the Mn to Al ratios. The higher concentration of Mn in the preliminary Mn–Al–C along with the larger atomic radius of Mn than Al intrigues Mn atoms to replace Al sites in the structure [29–31]. Consequently, the tetragonal distortion would increase compared to that of the conventional τ -phase. Also, the higher ordering in Mn–Al–C compared to the nanocomposite annealed at 300 °C may be due to the strain relief completed by the secondary ball-milling at 300 °C. Variations in lattice parameters which were discussed here can be seen in Table 1.

In Fig. 3a–d, optical microscope images of hard-soft $\text{Mn}_{52}\text{Al}_{45.7}\text{C}_{2.3}$ - α -Fe nanocomposite magnets, pressed under vertical uniaxial pressure and then sintered at different temperatures, have been illustrated. At lower temperatures such as 300 and 400 °C, samples resemble flat elliptic flakes which comprise grains with an average length of 20 μm and an average width of 5 μm (see the inset of Fig. 3a, b) This can cause grain anisotropy and better magnetization and/or coercivity. By contrast, at higher T , they change into amorphous due to dramatic grain growth (see the inset of

Fig. 3c, d). This diminishes anisotropy features in hybrid nanoparticles.

3.1 Magnetic Characterization

Magnetic hysteresis loops of $\text{Mn}_{52}\text{Al}_{45.7}\text{C}_{2.3}$, α -Fe, $\text{Mn}_{52}\text{Al}_{45.7}\text{C}_{2.3}$ - α -Fe, annealed at different temperatures, in Fig. 4 show single hard phase $\text{Mn}_{52}\text{Al}_{45.7}\text{C}_{2.3}$ has the highest coercivity and lowest magnetization. In $\text{Mn}_{52}\text{Al}_{45.7}\text{C}_{2.3}$ -10% α -Fe nanocomposite annealed at 400 °C, magnetization increases and coercivity decreases. Strikingly, the loop curve becomes demagnetized smoothly with no apparent kink implying the effective exchange coupling between hard $\text{Mn}_{52}\text{Al}_{45.7}\text{C}_{2.3}$ and soft α -Fe components. However, when the annealing temperature is further increased, the magnetic characteristics of loops decrease which can be attributed to the deterioration of exchange coupling with larger grain size at higher temperatures [19].

This also can best be followed in $\text{Mn}_{52}\text{Al}_{45.7}\text{C}_{2.3}$ hard phase for which the highest values of magnetic characteristics M_s , M_r , H_c emerge at 400 °C (Fig. 5).

This scenario is also backed by maximum energy product $(\text{BH})_{\text{max}}$ as a figure of merit of permanent magnets shown in Fig. 6. As seen, compositing $\text{Mn}_{52}\text{Al}_{45.7}\text{C}_{2.3}$ with α -Fe results in higher $(\text{BH})_{\text{max}}$ when annealed at 400 °C is indicative of the magnetic exchange coupling between $\text{Mn}_{52}\text{Al}_{45.7}\text{C}_{2.3}$ and α -Fe.

The magnetic exchange coupling in $\text{Mn}_{52}\text{Al}_{45.7}\text{C}_{2.3}$ - α -Fe nanocomposites can be further investigated by taking the derivative of magnetic hysteresis loop (Fig. 7) and Henkel plots (Fig. 8). In Fig. 7, the derivative magnetic curve, dM/dH vs H for single-phase $\text{Mn}_{52}\text{Al}_{45.7}\text{C}_{2.3}$ displays a

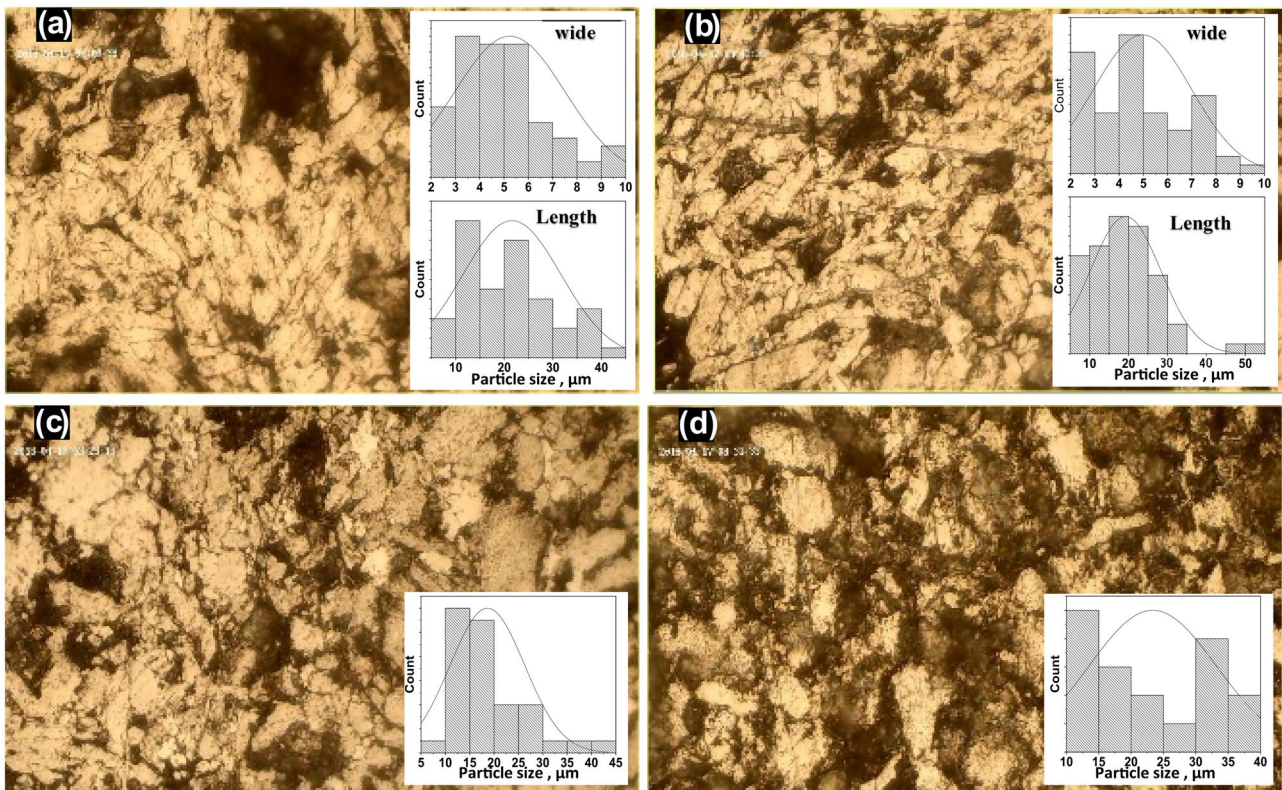


Fig. 3 a–d Optical microscope images for $\text{Mn}_{52}\text{Al}_{45.7}\text{C}_{2.3}$ - α -Fe nanocomposite magnets annealed at $T \sim 300$ – 600 °C inset with histogram distribution of the grain size

Fig. 4 Magnetic hysteresis loops for $\text{Mn}_{52}\text{Al}_{45.7}\text{C}_{2.3}$ - α -Fe nanocomposite magnets annealed at $T \sim 300$ – 600 °C. The inset shows hysteresis loops for $\text{Mn}_{52}\text{Al}_{45.7}\text{C}_{2.3}$ hard phase and α -Fe soft phase

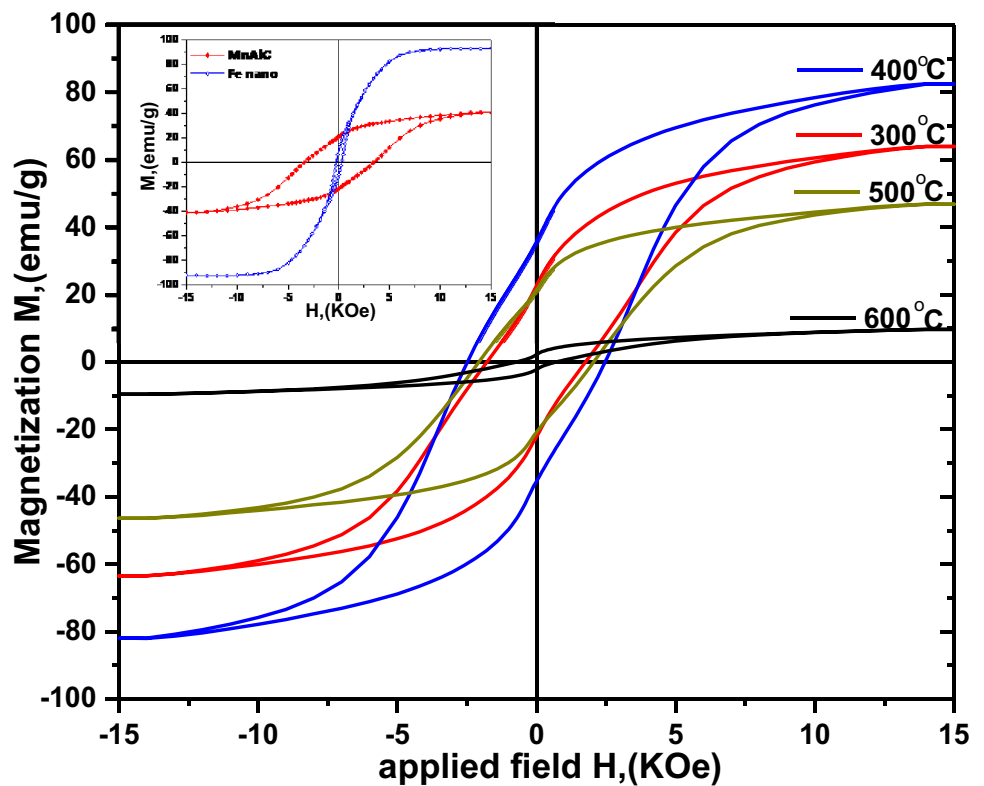
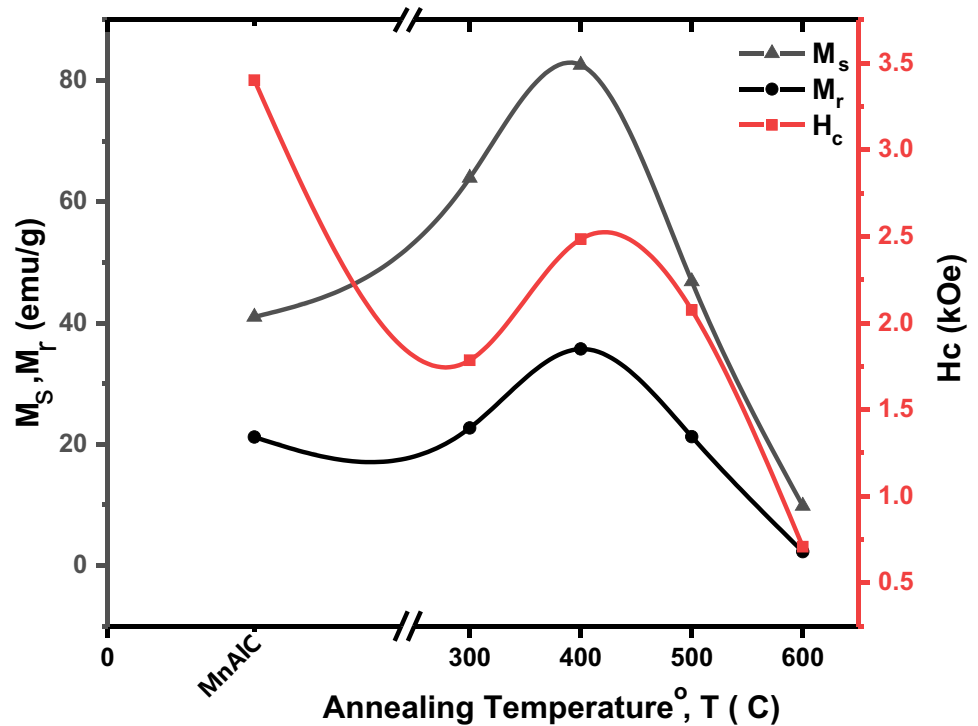


Fig. 5 The magnetic characteristics M_s , M_r , H_c values for $\text{Mn}_{52}\text{Al}_{45.7}\text{C}_{2.3}$ - α -Fe nanocomposite magnets annealed at $T \sim 300$ – 600 °C



maximum at 5 kOe relating to switching field of hard grains. The sort of weak and broad peak might be due to magnetostatic interaction competing with anisotropy field of the hard phase. In case of nanocomposite particles, annealing

at 300 °C gives two maxima. The maximum around 0.2 kOe belongs to the uncoupled soft phase and the maximum around 3 kOe belongs to exchange-coupled portion of the nanocomposite. This is suggestive of a significant amount

Fig. 6 $(BH)_{\max}$ values for $\text{Mn}_{52}\text{Al}_{45.7}\text{C}_{2.3}$ hard phase and $\text{Mn}_{52}\text{Al}_{45.7}\text{C}_{2.3}$ - α -Fe nanocomposite magnets annealed at $T \sim 300$ – 600 °C

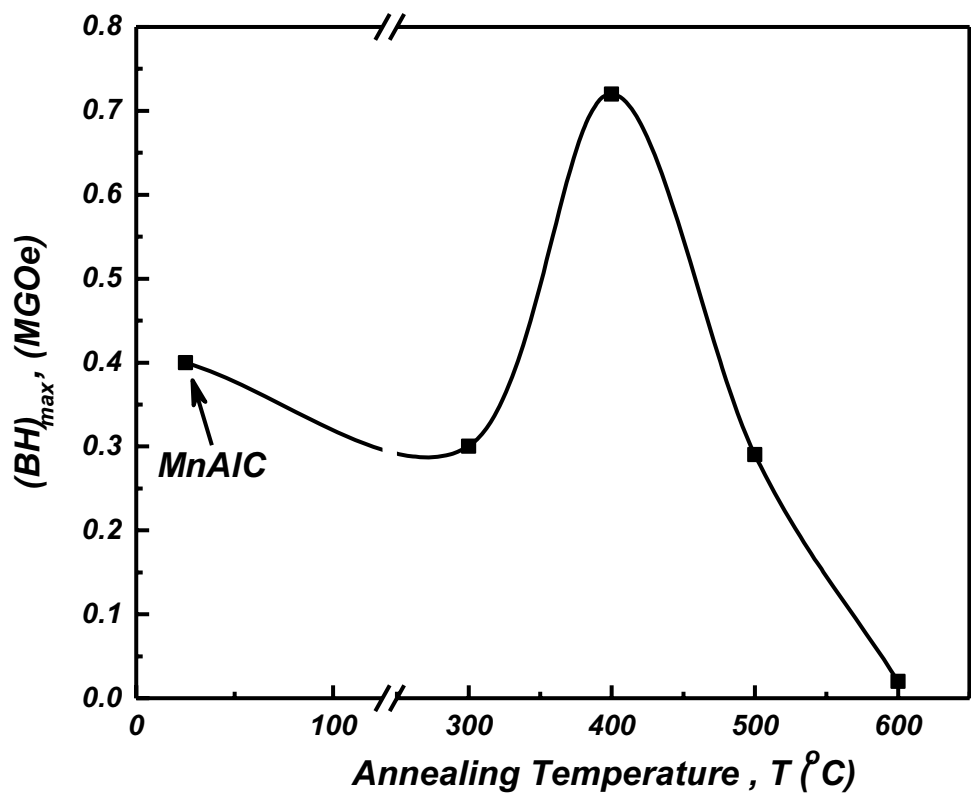
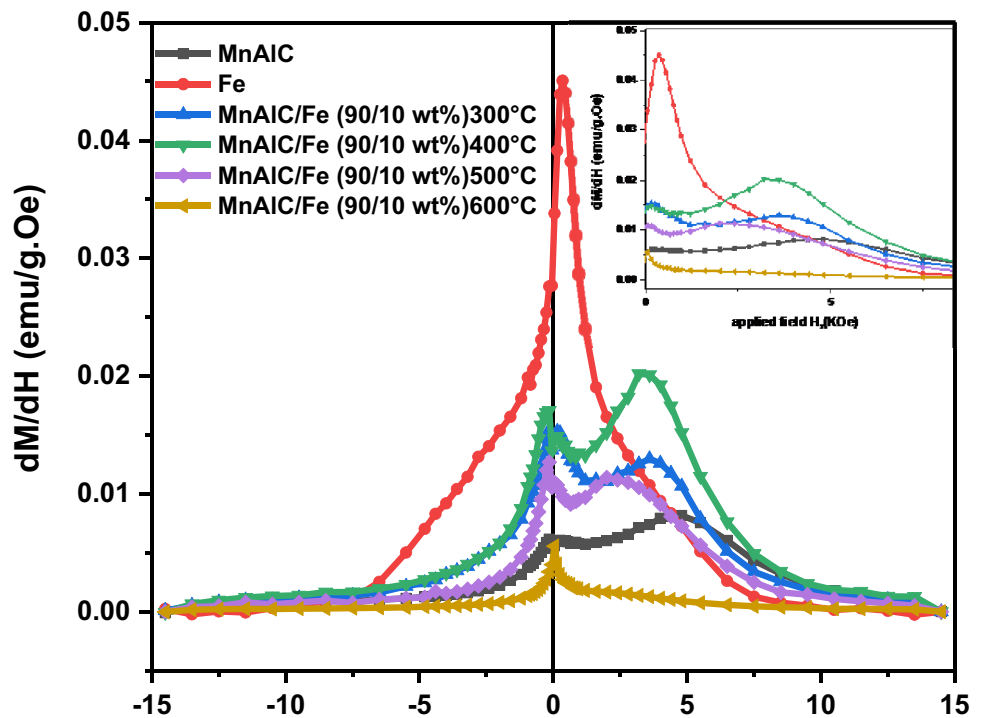


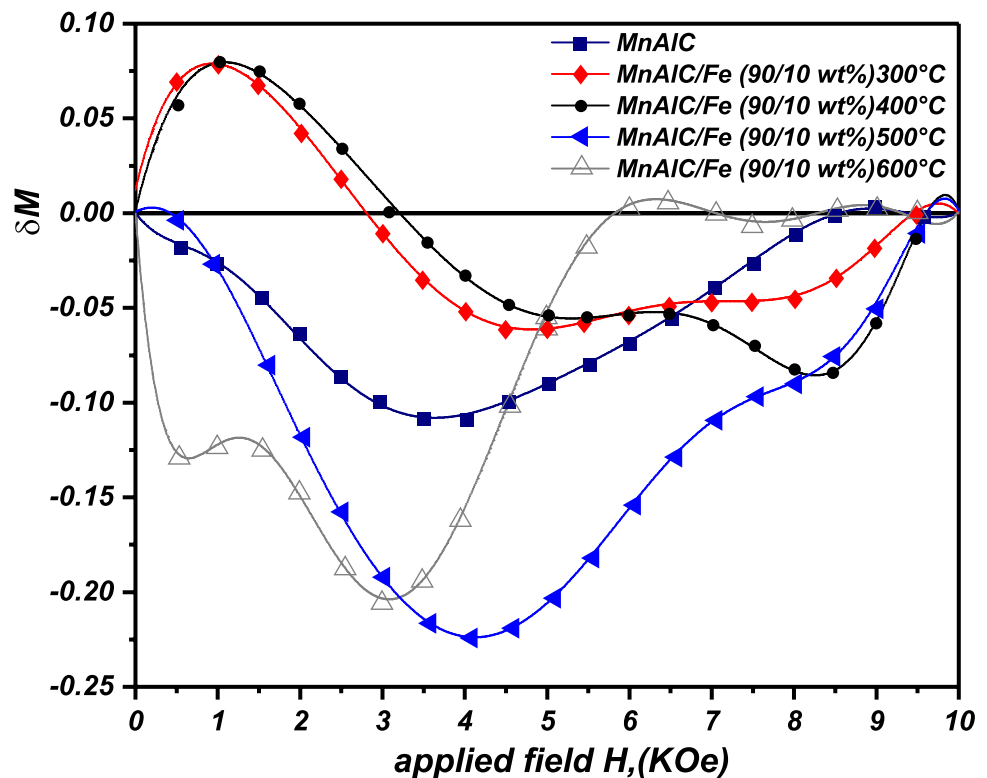
Fig. 7 Derivative hysteresis loops for $\text{Mn}_{52}\text{Al}_{45.7}\text{C}_{2.3}$, $\alpha\text{-Fe}$, $\text{Mn}_{52}\text{Al}_{45.7}\text{C}_{2.3}\text{-}\alpha\text{-Fe}$ nanocomposites annealed at $T \sim 300\text{--}600\text{ }^\circ\text{C}$. The inset illustrates low field region of derivative loops



of soft phase uncoupled with the hard phase. Increasing annealing temperature to $400\text{ }^\circ\text{C}$ leads to a smaller low field maximum that can be witnessed in the inset of Fig. 7 as strong evidence of exchange coupling enhancement between $\text{Mn}_{52}\text{Al}_{45.7}\text{C}_{2.3}$ and $\alpha\text{-Fe}$. One should note shifting of peaks

to lower fields at higher temperatures is due to the larger demagnetizing sites relating to $\alpha\text{-Fe}$ grains. At temperatures $500\text{ }^\circ\text{C}$ and higher, not many $\alpha\text{-Fe}$ grains would be fully coupled to hard $\text{Mn}_{52}\text{Al}_{45.7}\text{C}_{2.3}$ grains, and high field maximum in derivative curves would diminish.

Fig. 8 Henkel plots for $\text{Mn}_{52}\text{Al}_{45.7}\text{C}_{2.3}$, $\alpha\text{-Fe}$, $\text{Mn}_{52}\text{Al}_{45.7}\text{C}_{2.3}\text{-}\alpha\text{-Fe}$ nanocomposites annealed at $T \sim 300\text{--}600\text{ }^\circ\text{C}$



On the other hand, for Henkel plots, defined as: $M = M_d(H) - [1 - 2M_r(H)]$, where M_d stands for normalized demagnetization remanence, M_r stands for normalized isothermal magnetization remanence, and H stands for the applied magnetic field, the positive peak corresponds to exchange coupling interactions while the negative peak corresponds to magnetostatic interactions [16, 32–34]. In Fig. 8, the Henkel curve of $\text{Mn}_{52}\text{Al}_{45.7}\text{C}_{2.3}$ -10% α -Fe is dominated by a positive peak, a hallmark of effective exchange coupling interaction in nanocomposite particles. On the contrary, the Henkel curve of $\text{Mn}_{52}\text{Al}_{45.7}\text{C}_{2.3}$ is dominated with a negative peak, giving clear evidence of significant magnetostatic interactions between single-phase $\text{Mn}_{52}\text{Al}_{45.7}\text{C}_{2.3}$ grains. It should be noted that Henkel plot is a specific relation between the key parameters M_r , M_d ,

M_{inf} while knowing the magnetic interactions in permanent magnets with soft magnets, and so on. Therefore, analyzing Henkel plot would give a good insight into the interaction mechanism governing the magnetization of a magnetic material [35–39].

The magnetization reversal behavior for $\text{Mn}_{52}\text{Al}_{45.7}\text{C}_{2.3}$ - α -Fe nanocomposite magnets can be drawn from measuring recoil loops given in the insets of Fig. 9. Magnetization $M(H)$ and dc demagnetization remanence $M_d(H)$ curves as a function of the applied reversal field are given in Fig. 9. Based upon the micromagnetic model [19, 33], the exchange spring behavior corresponds with fully reversible magnetization and closed recoil demagnetization loops. For $T = 400^\circ\text{C}$, the ratio of H_r/H_c is significantly lower than the other temperatures and closer to Wohlfarth theoretical value ($H_r/H_c = 1.52$ displayed in the

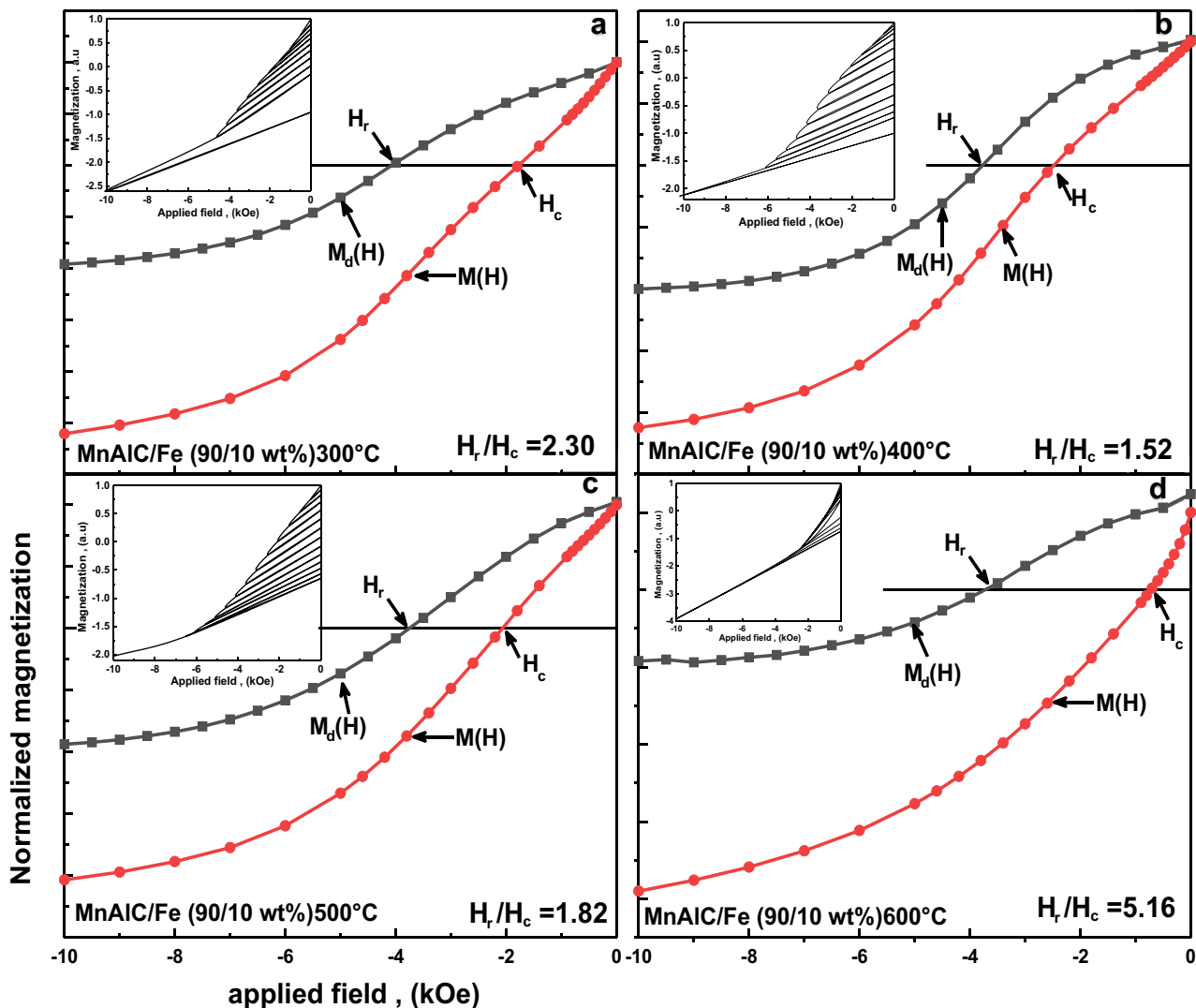


Fig. 9 Magnetization $M(H)$ and dc demagnetization $M_d(H)$ curves as a function of the reversal field for $\text{Mn}_{52}\text{Al}_{45.7}\text{C}_{2.3}$ - α -Fe nanocomposites annealed at $T \sim 300$ – 600°C . Lower insets display H_r/H_c ratio.

Recoil loops of demagnetization curves for nanocomposites annealed at different temperatures are shown in the insets also

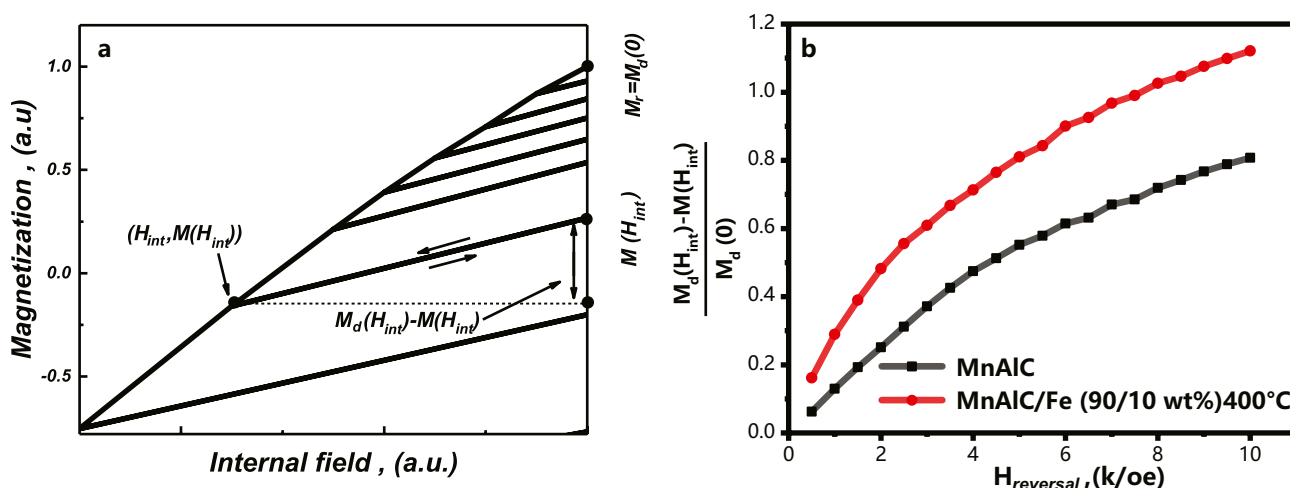


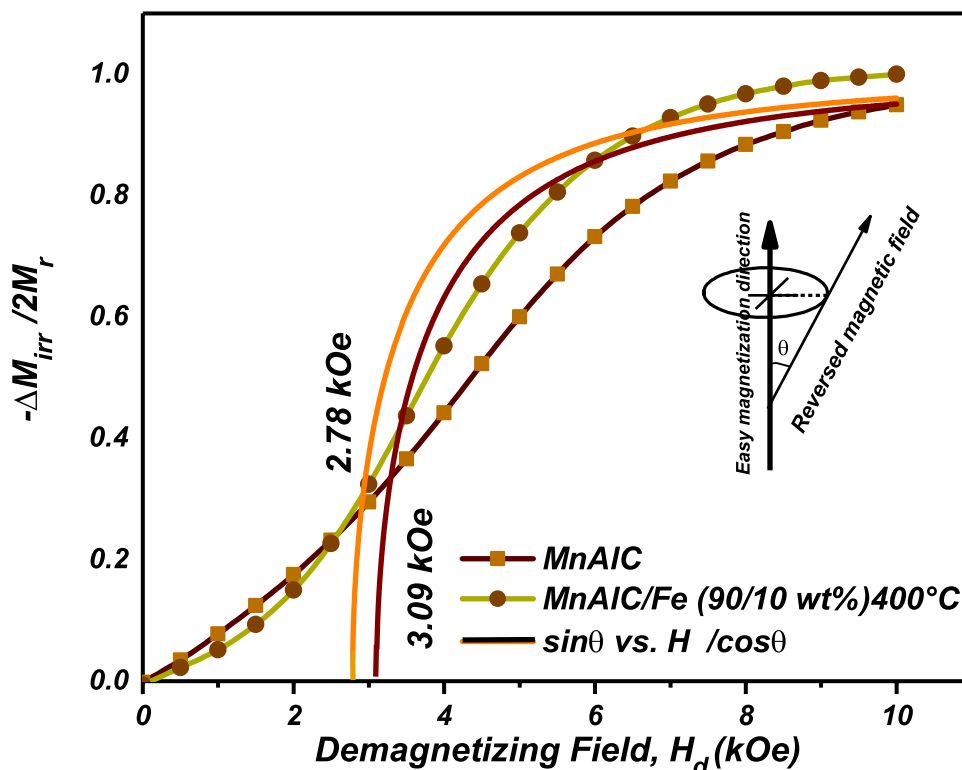
Fig. 10 **a** Representative recoil curves and the corresponding parameters are used in the text. **b** Comparison of normalized recovered magnetization $(M_d(H_{int}) - M(H_{int}))/M_d(0)$ as a function of the applied reversal field for $Mn_{52}Al_{45.7}C_{2.3}$ hard phase and $Mn_{52}Al_{45.7}C_{2.3}$ - α -Fe nanocomposites

lower inset). This is indicating soft grain switches coherently with hard grain like a single-phase alloy. It should be noted though, recoil loops are slightly open in this state (see the inset for $T=400^\circ\text{C}$). By contrast, temperatures other than 400°C give a larger gap between $M(H)$ and $M_d(H)$ curves, shown in the insets, as well as a wider opening of the recoil loops. H_r/H_c ratio is substantially larger than deviates from the prediction of micromagnetic model for randomly oriented uniaxial particles. This is representative of independent switching of the

hard- and soft-magnetic phase. Moreover, the integrated area of the recoil loop, as a criterion of energy loss in each cycle for $T=400^\circ\text{C}$, is significantly larger than that in other situations.

Moreover, recoil loops provide quantitative information on the recoverable magnetization. Corresponding recoil curves and empirical parameters used in this paper are illustrated in Fig. 10a. The change in recoverable magnetization $[M_d(H_{int}) - M(H_{int})]$, used in the relation after removing reversed field, is discussed in ref. [33] $M_d(0) = M_r$

Fig. 11 Dependence of $-\Delta M_{irr}/2M_r$ (H)/ $2M_r$ (∞) as a function of the applied reversal field for $Mn_{52}Al_{45.7}C_{2.3}$ hard phase and $Mn_{52}Al_{45.7}C_{2.3}$ - α -Fe nanocomposites. The nucleation field data H_n 3.091 kOe for $Mn_{52}Al_{45.7}C_{2.3}$ hard phase and 2.78 kOe for $Mn_{52}Al_{45.7}C_{2.3}$ - α -Fe nanocomposites are shown in the plot



is the remanence on the demagnetization curve. In Fig. 10b, normalized recoverable magnetization difference $M_d(H_{int}) - M(H_{int})/M_d(0)$ against the reversal field has been graphed for $T = 300\text{--}600\text{ }^\circ\text{C}$ in which a larger part of magnetization difference is recovered in nanocomposite annealed at $T = 400\text{ }^\circ\text{C}$. This is clear evidence of magnetic exchange coupling between $\text{Mn}_{52}\text{Al}_{45.7}\text{C}_{2.3}$ and $\alpha\text{-Fe}$.

Nucleation field H_n can be determined from irreversible magnetization $-\Delta M_{irrev}(H)$ of the hard phase in the form of reduced quantity: $-\Delta M_{irrev}(H)/2M_r = [M_r - M_d(H)]/2M_r$. According to Kondürsky model [33, 40–42], no detectable magnetization reversal arises unless reverse-field H reaches nucleation field H_n . Though, at reverse field $H_1 = H_n/\cos\theta_1$, magnetization reversal occurs in all regions with $0 \leq \theta \leq \theta_1$. Here, θ is the angle between the direction of reverse field and the easy axis of single-domain grains. The total irreversible change in magnetization is given $-\Delta M_{irrev} = 2M_r \int_0^{\theta_1} \cos\theta d\theta = 2M_r \sin\theta_1$. For details, see ref. [33]. The fitting of graphed $\Delta M_{irrev}(H)/2M_r$ curve by $\sin\theta$ against $H_n/\cos\theta_1$ gives nucleation field of 3.091 kOe for $\text{Mn}_{52}\text{Al}_{45.7}\text{C}_{2.3}$ hard phase and 2.78 kOe for $\text{Mn}_{52}\text{Al}_{45.7}\text{C}_{2.3}\text{-}\alpha\text{-Fe}$ nanocomposite magnets (see Fig. 11). The lower nucleation field for nanocomposite particles compared with the hard phase $\text{Mn}_{52}\text{Al}_{45.7}\text{C}_{2.3}$ is due to the exchange coupling between grains along with the enhancement of propagation of the magnetization reversal resulting in a reduced coercivity.

4 Conclusions

In summary, magnetic behaviors of ball-milled $\text{Mn}_{52}\text{Al}_{45.7}\text{C}_{2.3}\text{-}\alpha\text{-Fe}$ nanocomposite magnets annealed at different temperatures were investigated. The regular analysis of hysteresis curves reveals the best magnetic characteristics at $400\text{ }^\circ\text{C}$ with a smooth demagnetization curve, suggesting strong magnetic exchange coupling. This is approved by the variation of $(BH)_{max}$ for which nanocomposite particles annealed at $400\text{ }^\circ\text{C}$ provide the highest value. Additionally, derivative magnetic hysteresis curves, obtained for samples annealed at different temperatures, display the most intensity of characteristic variation peak at $400\text{ }^\circ\text{C}$, implying the dominant exchange coupling interaction between nanocomposite particles. Moreover, in the case of Henkel plots, the positive peak, a signature of magnetic exchange coupling interaction, was dominant for annealing at $400\text{ }^\circ\text{C}$ which obeys the trend revealed in other analyses, whereas the negative peak was dominant for others, suggesting dominant magnetostatic interaction between nanocomposite particles. Furthermore, information on recoverable magnetization as well as irreversible magnetization gives strong evidence of magnetic exchange coupling in nanocomposite particles annealed at $400\text{ }^\circ\text{C}$.

Acknowledgements The authors would like to acknowledge the kind support of the University of Tehran for the research work.

Declarations

Conflict of Interest The authors declare no competing interests.

References

- Chiriac, H., Marinescu, M., Tiberto, P., Vinai, F.: Reversible magnetization behavior and exchange coupling in two-phase NdFeB melt spun ribbons. *Mater. Sci. Eng. A* **304–306**, 957–960 (2001)
- Hirosawa, S., Kanekiyo, H.: Nanostructure and magnetic properties of chromium-doped Fe3B-Nd2Fe14B exchange-coupled permanent magnets. *Mater. Sci. Eng. A* **217–218**, 367–370 (1996)
- Kim, Y.J., Perepezko, J.H.: The thermodynamics and competitive kinetics of metastable τ phase development in MnAl-base alloys. *Mater. Sci. Eng. A* **163**(1), 127–134 (1993)
- Yang, S., Liu, X.S., Li, S.D., Xie, G.Z., Song, X.P., Gu, B.X., Du, Y.W.: Effect of wheel speed on the microstructure and exchange coupling interaction of nanocomposite Nd2Fe14B/ $\alpha\text{-Fe}$ magnets. *Mater. Sci. Eng. A* **347**(1), 325–329 (2003)
- Zhang, Y., Cui, C., Sun, J.-B., Yang, H.-X., Huanfang, T., Zhang, H., Li, J.Q.: Magnetic properties and microstructure of the dual-phase nanocomposite magnet $\text{Sm}_3(\text{Fe}, \text{Ti})_{29}\text{N}_x/\alpha\text{-Fe}$. *Mater. Sci. Eng. A* **433**, 90–93 (2006)
- Rong, C., Zhang, Y., Poudyal, N., Wang, D., Kramer, M.J., Liu, J.P.: Bulk $\text{SmCo}_5/\alpha\text{-Fe}$ nanocomposite permanent magnets fabricated by mould-free Joule-heating compaction. *J. Appl. Phys.* **109**(7), 07A735 (2011)
- Lisfi, A., Pokharel, S., Akioya, O., Alqhtany, N.H., Wuttig, M.: Irreversible magnetization process and switching mechanism in L10 FePt thin films. *AIP Adv.* **7**(5), 056206 (2017)
- Dorolti, E., Trifu, A.V., Isnard, O., Chicinaş, I., Tolea, F., Valeanu, M., Pop, V.: Influence of mechanical milling on the physical properties of $\text{SmCo}_5/\text{Fe}_6\text{Co}_3\text{5}$ type hard/soft magnetic nanocomposite. *J. Alloy. Compd.* **560**, 189–194 (2013)
- Ma, C.: Magnetic properties of exchange coupled $\text{SmCo}_5/\text{FeCo}$ composite particles synthesized by magnetic self-assembly. *Chem. Phys. Lett.* **696**, 31–35 (2018)
- Coey, J.M.D.: Hard magnetic materials: a perspective. *IEEE Trans. Magn.* **47**(12), 4671–4681 (2011)
- Coey, J.M.D.: Whither magnetic materials? *J. Magn. Magn. Mater.* **196**, 1–7 (1999)
- Martínez Sánchez, H., Zamora Alfonso, L.E., Trujillo Hernandez, J.S., Pérez Alcázar, G.A.: Evidence of exchange coupling in $\tau\text{-MnAlC}/\text{FeCo}$ system. *J. Magn. Magn. Mater.* **473**, 221–227 (2019)
- Hu, C., Pan, M., Wu, Q., Ge, H., Wang, X., Lu, Y., Pengyue, Z.: Effect of niobium addition on magnetization reversal behavior for SmCo -based magnets with TbCu_7 -type structure. *J. Rare Earths* **34**, 61–65 (2016)
- Wang, H.X., Si, P.Z., Jiang, W., Liu, J.J., Lee, J.G., Choi, C.J., Ge, H.L.: Structure and magnetic properties of $\text{MnAl}/\alpha\text{-Fe}$ nanocomposite powders prepared by high-energy ball milling. pp. 1492–1495. (2011)
- Pop, V., Gutoiu, S., Dorolti, E., Leostean, C., Isnard, O., Chicinas, I., Pana, O.: The influence of milling and annealing on the structural and magnetic behavior of $\text{Nd}_2\text{Fe}_{14}\text{B}/\alpha\text{-Fe}$ magnetic nanocomposite. *J. Alloy. Compd.* **581**, 821–827 (2013)
- Poudyal, N., Mohapatra, J., Xing, M., Kim, C.U., Liu, J.P.: High-temperature magnetic properties of exchange-coupled Sm-Co/Nd-Fe-B hybrid nanocomposite magnets. *IEEE Magn. Lett.* **9**, (2017)

17. Qian, H.-D., Si, P.-Z., Lim, J.T., Kim, J.-W., Park, J., Choi, C.-J.: Magnetic properties of Mn₅₄Al₄₆C₂₄₄/Sm₂Fe₁₇N₃ and Mn₅₄Al₄₆C₂₄₄/Fe₆₅Co₃₅ composites. *J. Korean Phys. Soc.* **73**(11), 1703–1707 (2018)
18. Cui, J., Kramer, M., Zhou, L., Liu, F., Gabay, A., Hadjipanayis, G., Balasubramanian, B., Sellmyer, D.: Current progress and future challenges in rare-earth-free permanent magnets. *Acta Mater.* **158**, 118–137 (2018)
19. Kneller, E.F., Hawig, R.: The exchange-spring magnet: a new material principle for permanent magnets. *IEEE Trans. Magn.* **27**(4), 3588–3600 (1991)
20. Xu, X., Hong, Y.-K., Park, J., Lee, W., Lane, A.M., Cui, J.: Magnetic self-assembly for the synthesis of magnetically exchange coupled MnBi/Fe–Co composites. *J. Solid State Chem.* **231**, 108–113 (2015)
21. Zeng, H., Li, J., Liu, J.P., Wang, Z.L., Sun, S.: Exchange-coupled nanocomposite magnets by nanoparticle self-assembly. *Nature* **420**(6914), 395–398 (2002)
22. Hernandez, J.S.T., Maccari, F., Marshall, L.G., Tabares, J.A., Alcázar, G.A.P.: Exchange coupling in MnAlC/ α -Fe nanocomposite magnets. *J. Supercond. Novel Magn.* **31**(12), 3941–3947 (2018)
23. Bazine, W., Tahiri, N., Omar, E.B., Ez-Zahraouy, H., Benyoussef, A.: Structural, electronic, magnetic, and magnetocaloric properties in intermetallic compound TbCu₂Si₂. *J. Magn. Magn. Mater.* **481**, (2019)
24. Ennassiri, N., Tahiri, N., El Bounagui, O., Ez-Zahraouy, H., Benyoussef, A.: Magnetic, magnetocaloric and transport properties in AlCMn₃ antiperovskite compound. *J. Alloy. Compd.* **741**, 1196–1202 (2018)
25. Jabar, A., Tahiri, N., Bahmad, L., Benyoussef, A.: A non-magnetic spacer layer effect on spin layers (7/2,3) in a bi-layer ferromagnetic dendrimer structure: Monte Carlo study. *Physica A* **462**, 1067–1074 (2016)
26. Tong, X., Sharma, P., Makino, A.: Investigations on low energy product of MnAl magnets through recoil curves. *J. Phys. D Appl. Phys.* **53**(17), 175001 (2020)
27. Sato, S., Irie, S.: Metamagnetic behavior in L10-MnAl synthesized by the post annealing of electrodeposited MnAl powder. *AIP Adv.* **9**(3), 035015 (2019)
28. Koch, A.J.J., Hokkeling, P., vd Steeg, M.G., Vos, K.J.D.: New material for permanent magnets on a base of Mn and Al. *J. Appl. Phys.* **31**(5), 75–77 (1960)
29. Jimenez-Villacorta, F., Marion, J., Oldham, J., Daniil, M., Willard, M., Lewis, L.: Magnetism-structure correlations during the epsilon \rightarrow tau transformation in rapidly-solidified MnAl nanostructured alloys. *Metals* **4**, 8 (2014)
30. Slater, J.C.: Atomic radii in crystals. *J. Chem. Phys.* **41**(10), 3199–3204 (1964)
31. Clementi, E., Raimondi, D.L., Reinhardt, W.P.: Atomic screening constants from SCF functions. II. Atoms with 37 to 86 Electrons. *J. Chem. Phys.* **47**(4), 1300–1307 (1967)
32. You, J., Guo, Y.: Plasma enhanced atomic layer deposition of Co thin film on τ -MnAl for effective magnetic exchange coupling and enhanced energy products. *J. Alloy. Compd.* **758**, 116–121 (2018)
33. Zhang, P.Y., Hiergeist, R., Lüdke, J., Albrecht, M., Ge, H.L.: Magnetization reversal behavior in high coercivity Zr doped α -Fe/Nd₂Fe₁₄B nanocomposite alloys. *J. Appl. Phys.* **108**(4), 043905 (2010)
34. Zhang, P., Pan, M., Ge, H., Yue, M., Liu, W.: Study on magnetization reversal behavior for annealed Nd₂Fe₁₄B/ α -Fe nanocomposite alloys. *J. Rare Earths* **31**(8), 759–764 (2013)
35. Ji, T.-C., Pan, M.-X., Ge, H.-L., Wu, Q., Zhang, P.-Y.: Magnetization reversal behavior and first-order reversal curve diagrams in high-coercivity Zr-doped α -Fe/Nd₂Fe₁₄B nanocomposite alloys. *Rare Met.* **40**(5), 1232–1238 (2021)
36. Geng, K.W., Pan, F., Yao, R.H.: Henkel analysis of Fe/Er multilayers prepared by electron-beam evaporation. *J. Appl. Phys.* **104**(7), 073902 (2008)
37. Basso, V., Bertotti, G.: Description of magnetic interactions and Henkel plots by the Preisach hysteresis model. *IEEE Trans. Magn.* **30**(1), 64–72 (1994)
38. Chwastek, K.: Description of Henkel plots by the magnetization-dependent Jiles-Atherton model. *J. Magn. Magn. Mater.* **322**(2), 214–217 (2010)
39. Patel, K., Zhang, J., Ren, S.: Rare-earth-free high energy product manganese-based magnetic materials. *Nanoscale* **10**(25), 11701–11718 (2018)
40. Sabirianov, R.F., Kashyap, A., Skomski, R., Jaswal, S.S., Sellmyer, D.J.: First principles study of transition-metal substitutions in Sm–Co permanent magnets. *Appl. Phys. Lett.* **85**(12), 2286–2288 (2004)
41. Yang, Y.B., Chen, X.G., Guo, S., Yan, A.R., Huang, Q.Z., Wu, M.M., Chen, D.F., Yang, Y.C., Yang, J.B.: Temperature dependences of structure and coercivity for melt-spun MnBi compound. *J. Magn. Magn. Mater.* **330**, 106–110 (2013)
42. Dehghan, H., Rezayat, M., Ebrahimi, S.A.S.: Modeling of strain induced transformation during hot deformation of an Mn–Al–C alloy. *Mat. Sci. Eng. A* **776**, 139006 (2020)

Publisher's Note Springer Nature remains neutral with regard to jurisdictional claims in published maps and institutional affiliations.